ELLIPTIC GRIDS WITH NEARLY UNIFORM CELL AREA AND LINE SPACING[*]

VIANEY VILLAMIZAR[†] AND SEBASTIAN ACOSTA[‡]

Dedicated to Víctor Pereyra on the occasion of his 70th birthday

Abstract. Two new quasi-linear elliptic systems of partial differential equations to automatically generate two-dimensional boundary conforming structured grids are formulated. One of the new systems generates grids with near-uniform cell areas. The other produces meshes with near-uniform coordinate line spacings. In both cases, the resulting grids conform to complex boundaries with severe singularities without self-overlapping. In contrast with other elliptic generators, the control functions are held as dependent variables. They obey Poisson-type equations with appropriate forcing. Grid quality analysis reveals the advantage in terms of smoothness and cell area uniformity of the new grids compared with other structured grids. An efficient procedure to combine the novel elliptic grids with algebraic grids for large domains is devised.

Key words. elliptic grids, control functions, smoothness, complex geometries, nearly uniform cell area, nearly uniform grid line spacing, mixed grids.

AMS subject classifications. 65N50; 65D10; 35J60

1. Introduction. The first successful elliptic grid generator consisted of a homogeneous system of two quasi-linear elliptic partial differential equations (PDE). It was derived by Winslow in the late sixties and its definition is given in his seminal paper [22]. The coordinates of the grid points were the unknown functions of the PDE system. They were numerically obtained by solving a Dirichlet boundary value problem governed by Winslow's equations. The most attractive feature of these grids is their smoothness. However, a major drawback is that there is no control of the location of grid lines. Undesired clustering of grid points normally occurs around the inner boundaries of multiple connected domains. In contrast, large spacing between grid lines is usually observed in the neighborhood of the outer boundaries. As a consequence, cells that are excessively small (inner region) or excessively large (outer region) are obtained. Inappropriately small cells cause instabilities for numerical methods employed in the computation of field variables, while excessively large cells are responsible for inaccurate approximations. Numerous works to establish control of the grid line locations have appeared in recent years. A good summary of these techniques can be found in Chapter 8 of the book by Hansen et al. [8] and the Handbook of Grid Generation by Thompson et al. [19].

In a recent work [20], we added grid line control to commonly used elliptic grid generator systems by introducing the Branch Cut Grid Control (BCGC) technique. For multiple connected domains with a single hole, O-type grids with cells of appropriate size for computation of field variables were generated. Control of the spacing between grid lines was established from a smooth initial distribution of grid points along the boundaries of the region, followed by definition of the control functions ϕ and ψ from this initial distribution. High quality grids were produced which contributed to the stability of explicit finite difference schemes used to compute the long-time simulation of annular vibrating membranes. In a subsequent work [21], the BCGC grids were successfully employed in the computation of pressure fields for several acoustic scattering problems.

The technique developed in [20] was extended to multiply-connected domains with more than one hole in [2]. The new algorithm was based on the decomposition of the original domain into nested sub-domains or blocks, each one containing a single hole. Then, the BCGC technique was applied to obtain an independent grid for each block, after which a smoothness process was implemented to smooth the block interfaces. As a result, globally smooth grids for domains with multiple holes were obtained. These new grids were also successfully tested over a variety of multiply connected domains by numerically solving problems of acoustic scattering from multiple obstacles [4]. Depending on the geometrical characteristics of the region, some undesired separation of grid lines at certain locations occurred after the generation. Therefore, a posteriori adjustment of the control functions was required to improve the quality of the BCGC grid generated.

In the present work, a detailed derivation and grid quality analysis of two novel elliptic grid generator models is performed. For one of them, the motivation is to automatically generate grids controlling the area of the cells, while the other one seeks to control the grid line separation along the curvilinear coordinates. Their most relevant feature is that the control functions ϕ and ψ are not determined beforehand as usual. Instead, they are part of the unknowns for a quasi-linear elliptic system of four partial differential equations. More precisely, they obey Poisson-type equations with appropriate forcing.

These grids were briefly introduced and used for the computation of acoustic scattering pressure fields in [1, 3]. To the best of our knowledge, there is not any previous treatment where the commonly used elliptic generating system has been extended to four equations including two more elliptic equations for the control functions. An advantage of doing this is that the generation process is fully automatic. But more importantly, the control functions automatically adjust themselves during the generation process to produce grids satisfying desired geometrical properties that will be discussed in more detail in the following sections.

2. Control functions and distribution of grid lines. Classical elliptic grid generators can be considered as a transformation T from a computational domain $\mathcal{D}'$ with rectangular coordinates (ξ, η) ($1 \leq \xi \leq N_1$ and $1 \leq \eta \leq N_2$), to the physical domain $\mathcal{D}$ with curvilinear coordinates $(x(\xi,\eta), y(\xi,\eta))$. The transformation T is defined by numerically solving a Dirichlet boundary value problem governed by the familiar quasi-linear elliptic system of partial differential equations [13, 19, 20] given by

$$\alpha x_{\xi\xi} - 2\beta x_{\xi\eta} + \gamma x_{\eta\eta} = -\alpha\psi(\xi,\eta)\, x_\xi - \gamma\phi(\xi,\eta)\, x_\eta, \qquad (2.1)$$

$$\alpha y_{\xi\xi} - 2\beta y_{\xi\eta} + \gamma y_{\eta\eta} = -\alpha\psi(\xi,\eta)\, y_\xi - \gamma\phi(\xi,\eta)\, y_\eta. \qquad (2.2)$$

The symbols α, β and γ represent the scale metric factors of the coordinate transformation. They are defined as $\alpha = x_\eta^2 + y_\eta^2$, $\beta = x_\xi x_\eta + y_\xi y_\eta$, $\gamma = x_\xi^2 + y_\xi^2$. The Jacobian J of the transformation T is given by $J = x_\xi y_\eta - x_\eta y_\xi$. The functions ψ and ϕ play an important role in the geometrical aspects of the cells of elliptic grids. For this reason, they are called grid control functions.

The control functions are normally defined before the generation process starts. Two main approaches follow. One consists of defining the control functions from the initial distribution of mesh points. For instance in [6], they are defined from the initial node distribution and later iteratively adjusted during the generation process. More recently, effective clustering (or stretching) of grid lines at desired locations was obtained from corresponding clustering (or stretching) present in the initial distribution of nodes on a branch cut of the physical domain [2, 20]. This was possible for O-type grids on multiply connected regions with one or more holes even in the presence of boundary singularities. However, as described in the previous section, some posteriori grid generation parameter adjustments were required in some cases.

The other approach, described in detail in [19, Chapter 4], requires the introduction of a parameter space P and a definition of a "grid control map" from the computational domain $\mathcal{D}'$ to P. The definition of the grid control map is not simple, especially when generating smooth grids in the entire domain. In some cases, it is necessary to solve Laplace's equation for the parameters involved in the grid control map.

The focus of this work is on the strict automatic generation of high-quality grids based on controlling two important geometrical properties of the grid cells. One is the area of the cells and the other is the grid line separation along the curvilinear coordinates ξ and η, respectively. A fully automatic generation can be achieved by extending the generating elliptic system (2.1)–(2.2) to four equations and by letting the control functions ϕ and ψ be the two additional unknowns.

The definition of these new equations is motivated by the effects that changes of the control function values in (2.1)–(2.2) have on the distribution of the grid lines. To illustrate these effects, consider a uniformly spaced rectangular grid with step sizes $\Delta\xi = 1$ and $\Delta\eta = 1$ defined on the computational domain $\mathcal{D}'$. Discrete values for ξ and η are represented by $\xi_i = i\Delta\xi$ and $\eta_j = j\Delta\eta$, for $i = 1, \ldots N_2$ and $j = 1, \ldots N_1$, respectively. Also, $x_{i,j}$ and $y_{i,j}$ correspond to discrete values of $x(\xi_i, \eta_j) = x(i, j)$ and $y(\xi_i, \eta_j) = y(i, j)$, respectively. Discrete approximations for the other dependent variables are denoted accordingly.

In [2, 4], it was found that an increment of the ϕ-value at a given grid point produces a local displacement of the corresponding η-curves (η = constant) in the direction of increasing η (outward). Similarly, a decrement of ϕ-values brings the grid lines inwards in the direction of decreasing η. Moreover, the displacement of the η-curves is proportional to the magnitude of the changes experienced by ϕ. The relationship between changes of ψ values and displacement of ξ-curves (ξ = constant) is analogous.

The above statements are illustrated in Figure 2.1. The left grid A corresponds to values of the control functions at step k and at the point (ξ_i, η_j) given by $\phi^k(\xi_i, \eta_j)$ and $\psi^k(\xi_i, \eta_j)$. The intermediate grid B is obtained at a subsequent step $k + 1$ by increasing the value of ϕ at (ξ_i, η_j); more precisely, by requiring that $\phi^{k+1}(\xi_i, \eta_j) > \phi^k(\xi_i, \eta_j)$. The final grid C is obtained from the intermediate one after increasing the value of ψ, at (ξ_i, η_j), i.e, $\psi^{k+1}(\xi_i, \eta_j) > \psi^k(\xi_i, \eta_j)$.
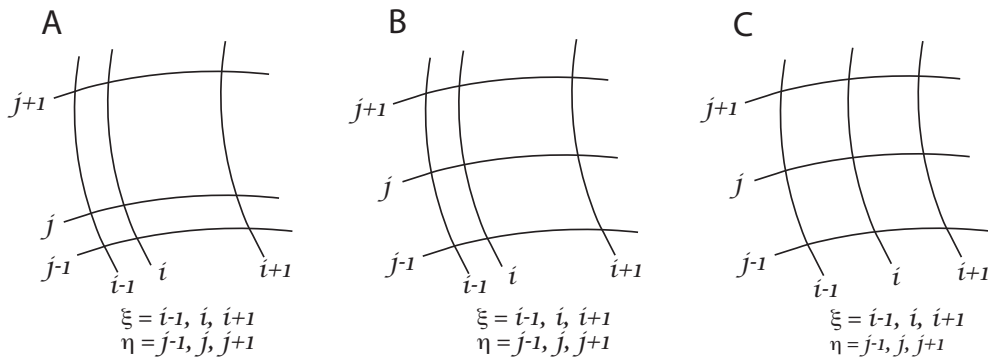

FIGURE 2.1. *Making grids with uniform area cells.* (A) ϕ_{ij}^k, ψ_{ij}^k (B) $\phi_{ij}^{k+1} > \phi_{ij}^k$ (C) $\psi_{ij}^{k+1} > \psi_{ij}^k$.

In the following sections, two new elliptic grid generating systems will be derived. The key idea in the formulation of the first one is to subject changes of the control functions ϕ and ψ at specific locations to relative changes of the area of consecutive cells at these locations.

For the second elliptic system, changes of ϕ and ψ at grid points are subjected to changes of the distance between consecutive grid points along the curvilinear coordinates ξ and η.

3. Grids with nearly uniform cell area: J-grids. The value of the Jacobian at a grid point provides an approximation of the area of the cell containing that point. This is illustrated in Figure 3.1(A) where a generic cell enclosing a region $\mathcal{R}$ is shown. The area of this region $A(\mathcal{R})$ can be approximated by $A(\mathcal{R}) \approx |\vec{X}_\xi \Delta\xi \times \vec{X}_\eta \Delta\eta|$ where $\vec{X} = (x(\xi, \eta), y(\xi, \eta))$, and $\Delta\xi = \Delta\eta = 1$. Therefore, $A(\mathcal{R}) \approx |x_\xi y_\eta - x_\eta y_\xi| = |J|$. As a consequence, near-uniform cell area meshes are equivalent to meshes with near constant Jacobian at all nodes.

A common method to numerically solve the generating quasi-linear elliptic system of PDEs (2.1)–(2.2) is to use an iterative method [4, 8, 19, 20]. From the previous paragraph, we conclude that if the Jacobian gradient were required to approach zero at every node at the end of the iteration process, then a final nearly uniform cell area grid could be obtained. This observation, together with the relationship between values of ϕ and ψ with displacement of grid lines (described in the previous section), suggests using the components of the gradient (J_ξ, J_η) as regulatory terms for the values of the control functions during the iteration process. In particular, it leads to a consideration of the following discrete equations for the control functions ϕ and ψ,

$$\phi_{ij}^{k+1} = \phi_{ij}^k + \frac{k_1}{4}\left(J_\eta\right)_{ij}^k, \tag{3.1}$$

$$\psi_{ij}^{k+1} = \psi_{ij}^k + \frac{k_2}{4}\left(J_\xi\right)_{ij}^k, \tag{3.2}$$

where $k_1 > 0$ and $k_2 > 0$ are real constants. Equation (3.1) states that values of the control function ϕ will increase (decrease) if derivatives in the direction of η of the Jacobian J are positive (negative). In practical terms, ϕ_{ij} will increase (decrease) if the area of the cell located at (ξ_i, η_{j+1}) is bigger (smaller) than the area of the one at (ξ_i, η_j). As a consequence, the common grid line of these two cells will move in such a way to decrease the difference between their areas (see Figure 2.1).

Equation (3.2) also states an analogous relationship between the motion of the grid lines at the interface of two neighboring cells along the ξ-direction and the control function ψ. As a consequence (see Figure 2.1) under rather general conditions, when equations (3.1)–(3.2) are coupled with the discrete approximation of the grid generation model governed by (2.1)–(2.2), and an iterative numerical method, such as point SOR [20], is used to solve all of them, then the area of all cells gradually tends to a near-constant value. In fact, the direction of the grid line displacements depends on the signs of J_η and J_ξ.
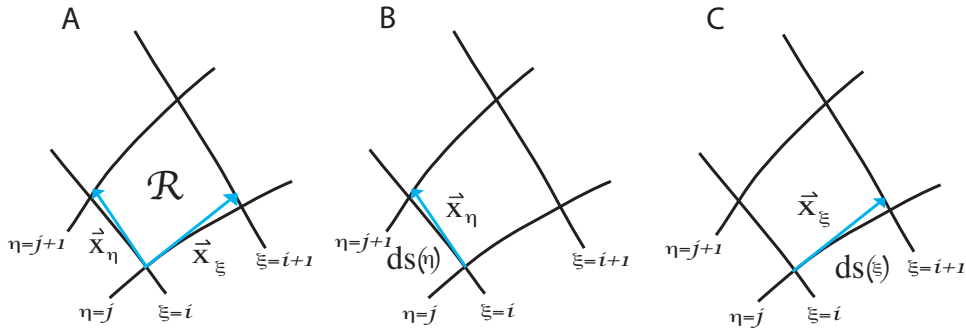

FIGURE 3.1. *(A) Cell area (B) Distance between ξ-curves (C) Distance between η-curves.*

A differential equation corresponding to (3.1) can be derived if values ϕ_{ij}^k are replaced by the average values of ϕ about the four neighboring points of (ξ_i, η_j), respectively. More precisely, equation (3.1) is replaced by

$$\phi_{i,j}^{k+1} = \frac{\phi_{i+1,j}^k + \phi_{i-1,j}^k + \phi_{i,j+1}^k + \phi_{i,j-1}^k}{4} + \frac{k_1}{4}(J_\eta)_{i,j}^k. \tag{3.3}$$

Now, by noticing that the term on the left and the first term on the right of (3.3) correspond to a second order central finite difference approximation of $\nabla^2_{\xi,\eta}\phi$, written in iterative form, the discrete equation (3.3) can be associated to the differential equation given by $\nabla^2_{\xi,\eta}\phi = -k_1 J_\eta$. Similarly, a continuous version of (3.2), $\nabla^2_{\xi,\eta}\psi = -k_2 J_\xi$, can be analogously obtained. By adding these two equations to the commonly used quasi-linear system (2.1)–(2.2), a new elliptic grid generation model is obtained

$$\alpha x_{\xi\xi} - 2\beta x_{\xi\eta} + \gamma x_{\eta\eta} = -\alpha\psi \, x_\xi - \gamma\phi \, x_\eta, \tag{3.4}$$

$$\alpha y_{\xi\xi} - 2\beta y_{\xi\eta} + \gamma y_{\eta\eta} = -\alpha\psi \, y_\xi - \gamma\phi \, y_\eta, \tag{3.5}$$

$$\phi_{\xi\xi} + \phi_{\eta\eta} = -k_1 J_\eta, \tag{3.6}$$

$$\psi_{\xi\xi} + \psi_{\eta\eta} = -k_2 J_\xi. \tag{3.7}$$

This is the first novel elliptic grid generator proposed in this work. It consists of the familiar elliptic equations (3.4)–(3.5) combined with Poisson type equations for the control functions. As described above, by forcing these new elliptic equations with the rate of change of the Jacobian along the curvilinear coordinate directions, it is possible to produce grids with near-uniform cell areas. Grids obtained by numerically solving the above system will be called J-grids in the remainder of this work. The effectiveness of the proposed new elliptic system is illustrated by several examples in the following sections.

4. Grids with nearly uniform line spacing: $\alpha\gamma$-grids. At a given grid point (x_{ij}, y_{ij}), the value $\sqrt{\alpha} = \sqrt{x_\eta^2 + y_\eta^2}$ denoted by $\sqrt{\alpha_{ij}}$ approximates the local distance between consecutive η-curves (η= constant). The arc length $ds(\eta)$ between two consecutive η-curves ($\eta = j$ and $\eta = j + 1$) is approximated by $ds(\eta) \approx \| \left(\vec{X}_\eta \right)_{ij} \Delta\eta \|$, where $\vec{X}_{ij} = (x_{ij}, y_{ij})$ and $\Delta\eta = 1$. Therefore,

$$ds(\eta) \approx \sqrt{(x_\eta)^2_{ij} + (y_\eta)^2_{ij}} = \sqrt{\alpha_{ij}}.$$

Similarly, the arc length between two consecutive ξ-curves ($\xi = i$ and $\xi = i + 1$) at $\vec{X}_{ij}$ may be approximated by the local value $ds(\xi) \approx \sqrt{\gamma}_{ij} = \sqrt{(x_\xi)^2_{ij} + (y_\xi)^2_{ij}}$. These facts are illustrated in Figure 3.1(B,C). They also suggest that meshes with near-equidistant η-curves and near-equidistant ξ-curves could be obtained by generating grids with their respective values of α and γ approximately equal at all nodes.

From the previous paragraph, we conclude that if $\alpha_\eta \approx 0$ and $\gamma_\xi \approx 0$ at every node at the end of the iteration process, then the spacing of the new coordinate lines will be near-uniform in the η-direction and ξ-direction, respectively. The above statements, together with the relationship between the values of ϕ and ψ and the displacement of coordinate lines at grid points, leads to a formulation of the following discrete equations

$$\phi_{ij}^{k+1} = \phi_{ij}^k + \frac{k_1}{4}(\alpha_\eta)_{ij}^k \quad \text{and} \quad \psi_{ij}^{k+1} = \psi_{ij}^k + \frac{k_2}{4}(\gamma_\xi)_{ij}^k. \tag{4.1}$$

By repeating the steps performed for the discrete equations (3.1)–(3.2) in the previous section, it is possible to show that equations (4.1) correspond to a discretization of the differential equations $\nabla^2_{\xi,\eta}\phi = -k_1\alpha_\eta$ and $\nabla^2_{\xi,\eta}\psi = -k_1\gamma_\xi$, respectively.

A new elliptic system is obtained by adding the continuous counterpart of (4.1) to (2.1)–(2.2). Hence, the second elliptic grid generation system of this work can be written as

$$\alpha x_{\xi\xi} - 2\beta x_{\xi\eta} + \gamma x_{\eta\eta} = -\alpha\psi\, x_\xi - \gamma\phi\, x_\eta, \tag{4.2}$$

$$\alpha y_{\xi\xi} - 2\beta y_{\xi\eta} + \gamma y_{\eta\eta} = -\alpha\psi\, y_\xi - \gamma\phi\, y_\eta, \tag{4.3}$$

$$\phi_{\xi\xi} + \phi_{\eta\eta} = -k_1\alpha_\eta, \tag{4.4}$$

$$\psi_{\xi\xi} + \psi_{\eta\eta} = -k_2\gamma_\xi. \tag{4.5}$$

Grids obtained by numerically solving this system will be called $\alpha\gamma$-grids.

Appropriate boundary conditions must be added to the new elliptic systems (3.4)–(3.7) and (4.2)–(4.5) before they can be used to generate grids. For the physical coordinate components x and y, these boundary conditions are, as usual, of Dirichlet type. They are defined by specifying an initial distribution of grid points along the physical boundaries $\eta = 1$ and $\eta = N_2$. In contrast, Neumann-type boundary conditions are imposed for the control functions ϕ and ψ. More precisely, they are free to change at the ends, i.e., $\phi_\eta = \psi_\eta = 0$, when $\eta = 1$ and $\eta = N_2$. For the coordinates x and y, as well as for the control functions ϕ and ψ, conditions of periodicity (or continuity) are imposed at the branch cut $\xi = 1$ and $\xi = N_1$. Therefore, the grid points at the branch cut are free to move, and they adjust during the generation process.

Grids obtained by using the elliptic system (4.2)–(4.5) certainly exhibit near-uniform coordinate line spacings, as shown in the following sections. In all our experiments, we will have $k_1 = k_2 = 1$. These choices for k_1 and k_2 will produce stable results in our numerical experiments. A more detailed analysis regarding the influence of values of k_1 and k_2 on the grid quality will be discussed at the end of Section 6.

5. Numerical method. The boundary value problems for the generation of J-grids and $\alpha\gamma$-grids described by the system of partial differential equations (3.4)–(3.7) and (4.2)–(4.5), respectively, are numerically solved. The technique employed in [20] for multiple connected domains with a single hole or as in [2, 4] for those domains with multiple holes is used. It consists of using centered finite difference approximation combined with point SOR iteration followed by a smoothness process. The only exceptions are in the approximations of ϕ_η and ψ_η at $\eta = 1$ and $\eta = N_2$, respectively, where one-sided second order finite differences are employed. As a result, a set of discrete equations is obtained. For the x component of the interior grid points $(x_{i,j}, y_{i,j})$, they are written in iterative form as follows

$$x_{i,j}^{k+1} = \frac{1}{2(\alpha+\gamma)_{i,j}}\left[\alpha_{i,j}\left(\left(1+\frac{\psi_{i,j}^k}{2}\right)x_{i+1,j}^k + \left(1-\frac{\psi_{i,j}^k}{2}\right)x_{i-1,j}^{k+1}\right) + \right. \tag{5.1}$$
$$\gamma_{i,j}\left(\left(1+\frac{\phi_{i,j}^k}{2}\right)x_{i,j+1}^k + \left(1-\frac{\phi_{i,j}^k}{2}\right)x_{i,j-1}^{k+1}\right)$$
$$\left. -\frac{\beta_{i,j}}{2}(x_{i+1,j+1}^k - x_{i+1,j-1}^k - x_{i-1,j+1}^{k+1} + x_{i-1,j-1}^{k+1})\right],$$

for $k = 1, 2, \ldots$, where

$$\alpha_{i,j} = ((x_\eta)_{i,j})^2 + ((y_\eta)_{i,j})^2, \qquad \beta_{i,j} = (x_\xi)_{i,j}(x_\eta)_{i,j} + (y_\xi)_{i,j}(y_\eta)_{i,j},$$
$$\gamma_{i,j} = ((x_\xi)_{i,j})^2 + ((y_\xi)_{i,j})^2, \qquad (x_\eta)_{i,j} = (x_{i,j+1}^k - x_{i,j-1}^{k+1})/2,$$
$$(y_\eta)_{i,j} = (y_{i,j+1}^k - y_{i,j-1}^{k+1})/2, \qquad (x_\xi)_{i,j} = (x_{i+1,j}^k - x_{i-1,j}^{k+1})/2,$$
$$(y_\xi)_{i,j} = (y_{i+1,j}^k - y_{i-1,j}^{k+1})/2, \qquad i = 2, \ldots, N_2 - 1, \quad j = 2, \ldots, N_1 - 1.$$

Completely analogous equations are obtained for the y component of the coordinate points.

Additionally, the discretized version of the Poisson-type equation for the control function ϕ at interior points is given by

$$\phi_{i,j}^{k+1} = \frac{\phi_{i+1,j}^k + \phi_{i-1,j}^{k+1} + \phi_{i,j+1}^k + \phi_{i,j-1}^{k+1}}{4} + \frac{k_1}{4}(J_\eta)_{i,j}^k, \qquad k = 1, 2, \ldots, \quad (5.2)$$

where

$$(J_\eta)_{i,j}^k = (x_{\xi\eta})_{i,j}(y_\eta)_{i,j} + (x_\xi)_{i,j}(y_{\eta\eta})_{i,j} - (x_{\eta\eta})_{i,j}(y_\xi)_{i,j} - (x_\eta)_{i,j}(y_{\xi\eta})_{i,j}$$

and

$$(x_{\eta\eta})_{i,j} = x_{i,j+1}^k - 2x_{i,j}^k + x_{i,j-1}^{k+1},$$
$$(y_{\eta\eta})_{i,j} = y_{i,j+1}^k - 2y_{i,j}^k + y_{i,j-1}^{k+1},$$
$$(x_{\xi\eta})_{i,j} = (x_{i+1,j+1}^k - x_{i-1,j+1}^{k+1} - x_{i+1,j-1}^k + x_{i-1,j-1}^{k+1})/4,$$
$$(y_{\xi\eta})_{i,j} = (y_{i+1,j+1}^k - y_{i-1,j+1}^{k+1} - y_{i+1,j-1}^k + y_{i-1,j-1}^{k+1})/4,$$

for $i = 2, \ldots, N_2 - 1$, $j = 2, \ldots, N_1 - 1$, while the other control function ψ is approximated by analogous formulas at grid points $(x_{i,j}, y_{i,j})$. The k and $k+1$ super-indices represent the current and the subsequent steps of the iterative process, respectively. At the boundary points, we discretize the Neumann-type boundary condition for the control functions using a second order one-sided finite difference formula. For instance at the inner boundary where $j = 1$, the following discrete equation is employed

$$\phi_{i,1}^{k+1} = (4\phi_{i,2}^k - \phi_{i,3}^k)/3. \qquad (5.3)$$

Similar equations are formulated for the control function ψ at boundary grid points.

The SOR method consists of the iteration of the previous discrete equations combined with an accelerating mechanism. The numerical values obtained at iteration $k+1$ are updated by using a linear combination of values at steps k and $k+1$. For instance, for the x-coordinate the updated values are defined by $x_{i,j}^{k+1} = \omega x_{i,j}^{k+1} + (1 - \omega)x_{i,j}^k$. Values of the relaxation parameter ω are in the interval $(0, 2)$. Also, the iteration process requires an initial grid. In Section 7, we will define typical algebraic initial grids. The iteration stops when the maximum distance between all corresponding points of two consecutive grids is less than a specified tolerance.

6. Grid quality analysis. In Figure 6.1, the generation of a nearly uniform cell-area 51×21 J-grid is illustrated for a five-cusps astroid domain. On the right hand side, changes in the control function ϕ, as the iteration progresses, are depicted. The relationship between changes of the ϕ values and the motion of the η-curves, discussed in Section 2, is observed. The cells with the smallest areas in the initial grid are located at the four cusps of the astroid, as shown at the top of Figure 6.1. It is precisely at these points where the control function ϕ grows more as the grid generation progresses. As a consequence, the separation of η curves close to the inner boundary is greatly increased with respect to the initial grid. This produces a final grid (bottom graph of Figure 6.1) whose cell areas are more uniform.
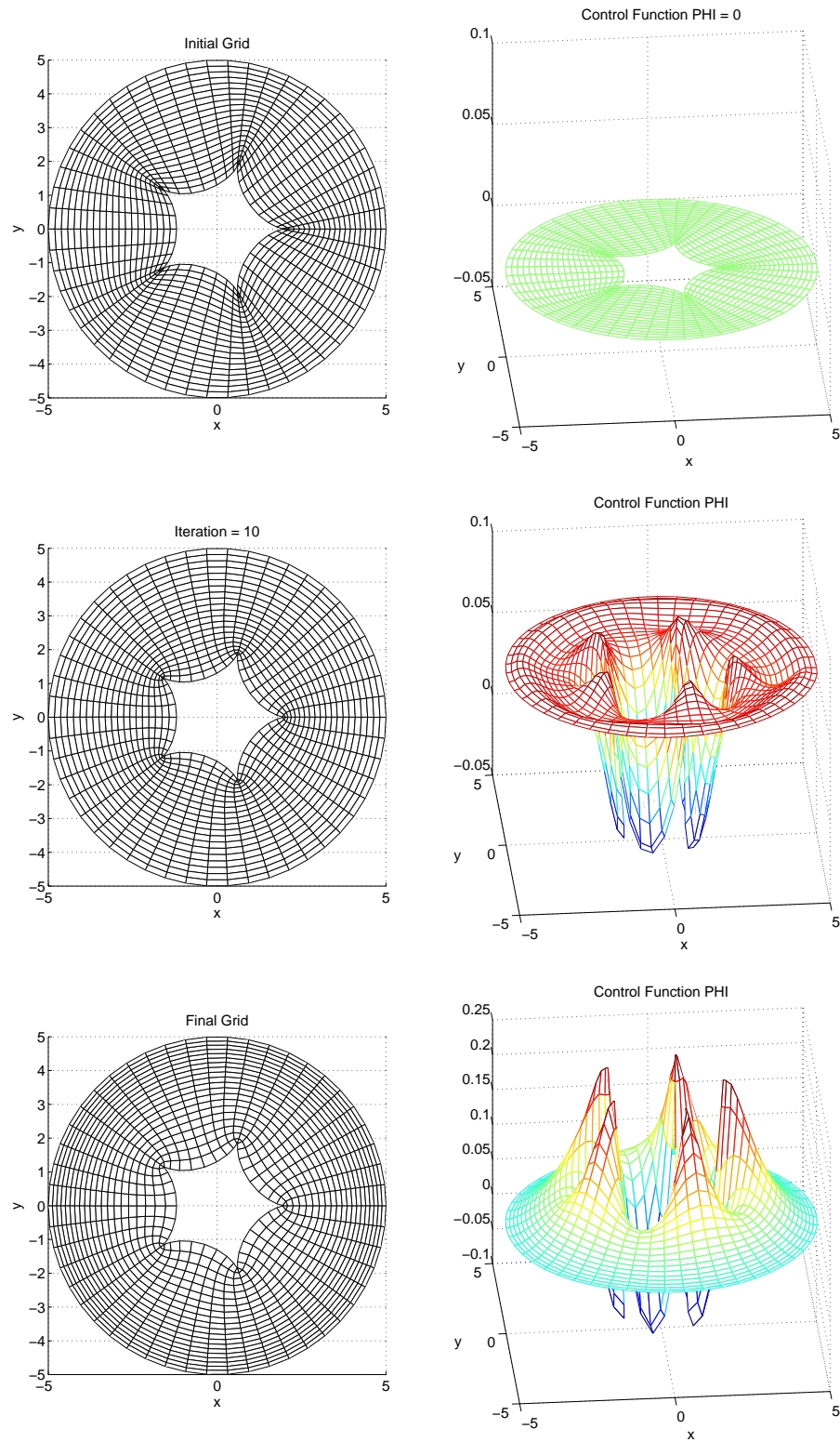
FIGURE 6.1. *Generation process for a J-grid. Effect of control function ϕ on the η-curves.*

TABLE 6.1
Jacobian comparison on different grids for five-cusp astroid domain.

Grid type	J_{min}			J_{max}		
	51×51	101×101	201×201	51×51	101×101	201×201
Winslow	1.14e-4	6.84e-6	4.14e-7	1.15e-1	2.88e-2	7.19e-3
BCGC	5.22e-4	2.11e-5	1.36e-6	5.76e-2	1.44e-2	3.58e-3
$\alpha\gamma$-Grid	6.93e-4	4.48e-5	2.39e-6	5.16e-2	1.30e-2	3.32e-3
J-Grid	6.61e-3	4.69e-4	2.73e-5	5.60e-2	1.36e-2	3.16e-3

6.1. Cell area. In Table 6.1, a comparison of the Jacobian for different grids of the same size for the five-cusps astroid domain of Figure 6.1 is made. As discussed in Section 3, the Jacobian value at a grid point serves to approximate the area of the corresponding grid cell. From the table values, it is observed how the difference between maximum and minimum values of J differs by a little over one order of magnitude for a J-grid, while for the others is mostly three order of magnitudes. Also, the minimum Jacobian is greater for J-grids. For instance, the minimum Jacobian for a 201×201 J-grid is almost two orders of magnitude larger than for a Winslow grid of the same size, and, almost one order of magnitude larger than a BCGC grid of the same size. There are physical problems where clusters of cells in certain locations are required for more accurate field computation. However, when the area of the cells fall below a threshold the grid lines may overlap, producing folded grids which are undesirable for field variable computations.

6.2. Smoothness. Another important grid property is smoothness. In [4], we measured smoothness by considering approximations of tangent vectors at every interior grid point $\mathbf{x}_{i,j} = (x_{i,j}, y_{i,j})$ along the η and ξ coordinate lines, respectively. For instance, along the ξ-direction the following backward and forward finite difference approximations are used for the tangent vector at $\mathbf{x}_{i,j} = (x_{i,j}, y_{i,j})$,

$$\mathbf{x}_\xi^{fwd}(\mathbf{x}_{i,j}) = \mathbf{x}_{i+1,j} - \mathbf{x}_{i,j}; \quad \mathbf{x}_\xi^{bwd}(\mathbf{x}_{i,j}) = \mathbf{x}_{i,j} - \mathbf{x}_{i-1,j}.$$

The angle $\kappa_{i,j}$ between $\mathbf{x}_\xi^{bwd}$ and $\mathbf{x}_\xi^{fwd}$ at the grid point $\mathbf{x}_{i,j}$ satisfies

$$\cos \kappa_{i,j} = \frac{\mathbf{x}_\xi^{bwd}(\mathbf{x}_{i,j}) \cdot \mathbf{x}_\xi^{fwd}(\mathbf{x}_{i,j})}{\| \mathbf{x}_\xi^{bwd}(\mathbf{x}_{i,j}) \| \, \| \mathbf{x}_\xi^{fwd}(\mathbf{x}_{i,j}) \|}.$$

A good measure of the smoothness at $\mathbf{x}_{i,j} = (x_{i,j}, y_{i,j})$ in the ξ-direction is given by the deviation of the angle $\kappa_{i,j}$ from the value zero. Therefore, the maximum deviation from smoothness (MDS) in the ξ-direction for a given grid can be defined as

$$\text{MDS}_\xi = max \ (\kappa_{i,j}), \qquad 1 \le i \le N_1 - 1, \qquad 2 \le j \le N_2 - 1,$$

and the average deviation from smoothness (ADS) in the ξ-direction as

$$\text{ADS}_\xi = \frac{1}{(N_1 - 1)(N_2 - 2)} \sum_{i=1}^{N_1-1} \sum_{j=2}^{N_2-1} \kappa_{i,j}.$$

Analogously, the maximum deviation from smoothness MDS_η and the average deviation from smoothness ADS_η in the η-direction, can be defined from one-sided finite difference approximations of the tangent vector at $\mathbf{x}_{i,j}$ in the η-direction.

In Table 6.2, MDS values for the five-cusps astroid domain of Figure 6.1 are reported for different types of grids of various sizes. For this particular domain, there are no major smoothness variations among the different grids along the η-direction. In the ξ-direction, however, maximum deviation from smoothness occurs on the first interior η-curve in the vicinity of the astroid's cusps. This is expected since the elliptic grids are trying to conform to the slope singularity present there. From the table values, the smoothness improvement experienced by J-grids in the ξ-direction compared with the others is noticeable.

TABLE 6.2
Maximum deviation from smoothness for the five-cusps astroid domain.

Grid type	MDS_ξ			MDS_η		
	51×51	101×101	201×201	51×51	101×101	201×201
Winslow	$109°$	$114°$	$116°$	$11.3°$	$12.0°$	$12.3°$
BCGC	$88.6°$	$92.4°$	$94.6°$	$12.9°$	$13.7°$	$14.0°$
$\alpha\gamma$-Grid	$72.8°$	$77.4°$	$83.2°$	$12.5°$	$13.6°$	$14.0°$
J-Grid	$33.0°$	$36.9°$	$41.2°$	$8.4°$	$12.0°$	$13.4°$

On the other hand, the sensitivity of the quality of the final grid to the constants k_1 and k_2 is shown in Table 6.3 on 51×51 grids for the five-cusps astroid domain. The grid quality parameters reported in the table are the minimum Jacobian value J_{min}, maximum Jacobian value J_{max}, maximum deviation from orthogonality (as defined in [7]) at the Astroid's boundary MDO_{bdy}, maximum deviation from smoothness along the ξ-direction MDS_ξ, and maximum deviation from smoothness along the η-direction MDS_η.

The last row of Table 6.3 contains the number of iterations needed for the process to converge to the final grid. As an initial guess for the SOR process, the control functions ϕ and ψ are set equal to zero. When $k_1 = k_2 = 0$ the control functions in equations (3.6) and (3.7) are not fed back from the gradient of the Jacobian, and therefore they remain zero through the entire iteration process. As a consequence, the case $k_1 = k_2 = 0$ corresponds to Winslow grids. This explains the relatively large difference between J_{min} and J_{max} in Table 6.3 for the case $k_1 = k_2 = 0$. But as long as the control functions are influenced by the Jacobian, i.e., when $k_1, k_2 > 0$, they iteratively adjust to produce grids of nearly uniform cell area.

Another important difference is observed for the parameter MDS_ξ: Winslow grids bend much more than J-grids at complex boundaries. The grid quality parameters show little variation for the nonzero values of k_1 and k_2, although it is noticeable that the number of SOR iterations increases with larger values of these constants. This is due to oscillations on the control function values at the early stages of the iterative process for larger values of k_1 and k_2.

Similar behaviors are observed for the sensitivity of the grid quality parameters with respect to variations of k_1 and k_2 for the $\alpha\gamma$-grids. Experiments for finer J-grids and $\alpha\gamma$-grids were also performed. It was found that larger k_1 and k_2 values lead to a divergent grid generation algorithm. For instance for the 51×51 grid of Table 6.3, the J-grid algorithm is divergent when $k_1, k_2 \geq 13$. Also for 101×101 J-grids, the generation algorithm diverges for values of $k_1, k_2 \geq 15$.

6.3. Orthogonality. Regarding orthogonality at the inner boundaries, for the J-grids and $\alpha\gamma$-grids over multiple connected regions with a single hole, the parameters MDO (maximum deviation from orthogonality) and ADO (mean deviation from orthogonality) introduced in [7] are used. In particular, they are calculated for the multiple connected domains described in Table 6.4 and depicted in Figure 6.2. These experiments illustrate that J-grids

TABLE 6.3
Sensitivity to the constants $k_{1,2}$ for the five-cusps astroid domain on a 51×51 J-grid.

	$k_1 = k_2 = 0.0$	$k_1 = k_2 = 0.5$	$k_1 = k_2 = 1.0$	$k_1 = k_2 = 1.5$
J_{min}	1.14e-4	6.19e-3	6.61e-3	6.76e-3
J_{max}	1.15e-1	5.99e-2	5.60e-2	5.59e-2
MDO_{bdy}	5.6°	3.9°	3.5°	3.4°
MDS_ξ	109°	39°	33°	31°
MDS_η	11.3°	8.2°	8.4°	8.4°
Iter	544	668	707	751

and $\alpha\gamma$-grids are near-orthogonal for domains without entrant corners such as the five-cusps astroid and the ellipse of Figure 6.2. However, for a singular domain with entrant corners such as the epicycloid (also shown in Figure 6.2), the deviation from orthogonality is large near the cusps. This is expected not only for the J and $\alpha\gamma$ algorithm but for any non-self-overlapping grid generator near this type of singularity. It is well known that simultaneously conditioning more than one property of the grid potentially results in clashing demands [12]. For example, in [5], it is shown that reducing the aspect ratio values may result in an increase in the mean deviation from orthogonality (ADO). In our case, the conforming and non-self-overlapping properties of the algorithms under study preclude the orthogonality about the cusps.

A well-known algorithm based on a system of two quasi-linear elliptic equations such as (2.1) and (2.2) that respects orthogonality at the boundary is called GRAPE (Grids about Airfoils using Poisson's Equation). The theory behind this algorithm is due to Steger and Sorenson, and can be found in [17]. It is intended for smooth boundaries. This algorithm certainly produces near-orthogonal grids for smooth boundaries, but it will face the same opposing demands (orthogonality versus non-self-overlapping) for singular boundaries as the one described by the epicycloid at the cusps. The GRAPE algorithm also produces grids with cells of non-uniform area similar to Winslow grids away from the boundaries. This may cause lack of accuracy for field computations in the interior regions.

TABLE 6.4
Deviation from orthogonality at boundary points for 101×101 J and $\alpha\gamma$-grids.

	Astroid		Ellipse		Epicycloid	
	J-grid	$\alpha\gamma$-grid	J-grid	$\alpha\gamma$-grid	J-grid	$\alpha\gamma$-grid
MDO_{bdy}	3.4°	3.2°	5.9°	4.8°	63.9°	58.5°
ADO_{bdy}	2.1°	2.0°	3.8°	2.6°	50.1°	42.2°

7. Mixed algebraic-J grids and mixed algebraic-$\alpha\gamma$ grids. Although it is possible to generate global J-grids and $\alpha\gamma$-grids for large domains, it may be computationally expensive in most practical applications. For large domains bounded by geometrically complex boundaries, it is more convenient to generate elliptic grids for a relatively small region surrounding the obstacle. For the remaining, geometrically simpler part of the domain, an algebraic generation method is usually good enough for field computations, and is much faster due to its explicit nature.

For geometrically complex domains, combination of generation techniques has become a common practice. For instance, this approach was followed by Sherer and Visbal [15], who employed overset grids as a support for the simulation of acoustic scattering from multiple cylinders. The overset technique employs interpolating polynomials to match a boundary-fitted grid around the obstacles with an algebraic Cartesian mesh covering the rest of the
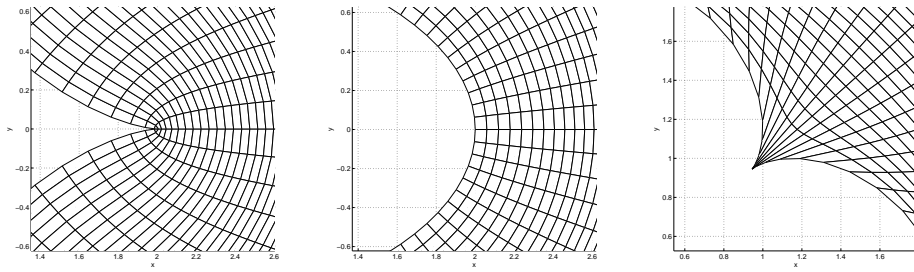
FIGURE 6.2. *Zoom on J-grids showing the deviation from orthogonality at boundary points.*

domain.

In this section, we construct some meshes for various complex domains. They consist of portions of J-grids or $\alpha\gamma$-grids for that part of the domain surrounding the the holes of multiple connected domains and algebraic meshes for the remaining parts. To start the process, an initial algebraic grid is generated. It is obtained by first defining an initial distribution of points along the physical boundaries (ξ-direction). Then, these boundary points are linearly interpolated inside the domain in the η-direction producing ξ-curves. Along each of these ξ-curves, piecewise uniform partitions with the same number of points are defined. Different step sizes are used for different segments of the ξ-curves. This means that nodes are locally uniformly distributed on each ξ-curve. Using these points, the grid η-curves are generated by linear interpolation along the ξ-direction, producing a final algebraic grid.

The resulting algebraic grids are illustrated at the left in Figure 7.1 and Figure 7.2 for two different domains. They conform to the boundaries but are generally non-smooth. They have very skewed cells around the boundary corner and cusps. Also, the abrupt changes from a small step size in the more dense region to the large step size in the intermediate region creates non-smoothness along the ξ-curves. Additionally, the complex bounding curves may induce self-overlapping of grid lines, and the propagation of slope discontinuities to the interior of the domain.

The new elliptic grid generators which are the subject of this work are now used to smooth the algebraic grids of Figures 7.1 and 7.2. The algorithm to generate J-grids is applied to the algebraic grid at the left in Figure 7.1 while the algorithm to generate $\alpha\gamma$-grids is applied to the algebraic grid at the left in Figure 7.2. However, they are applied only in the neighborhood of the boundaries, where the density of grid lines is greater (darker regions in the initial algebraic grid figures). As a result, grid properties such as orthogonality, line-smoothness, area-uniformity, and line-spacing are greatly improved within these regions.

Once the elliptic grids have been generated in the neighborhood of the boundaries (inner and outer), the portion of the algebraic grid occupying the intermediate region is regenerated. First, the distribution of points along the ξ-curves is redefined. This is done by interpolating the location of grid points from the two smoothed boundary regions to the intermediate region by means of Hermite polynomials of degree four. As a result, the abrupt changes from a small step size in the more dense regions to the large step size in the intermediate regions along the ξ-curves is replaced by a smooth changes in the step sizes. The new grid points along the ξ-curves are linearly interpolated along the ξ-direction producing an improved intermediate algebraic grid.

More detailed graphs of the initial algebraic grids and the final mixed grids are shown in Figures 7.3 and 7.4. There are noticeable smoothness improvements experienced by the cells
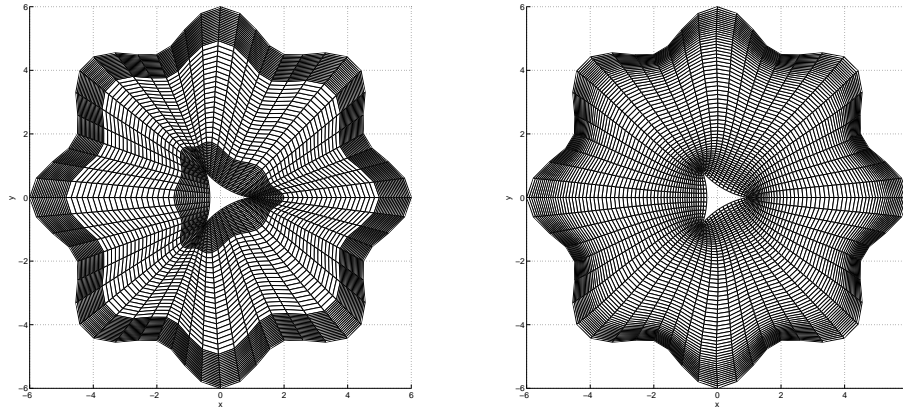
FIGURE 7.1. *Initial algebraic grid and final* 61×61 *mixed algebraic-J grid.*
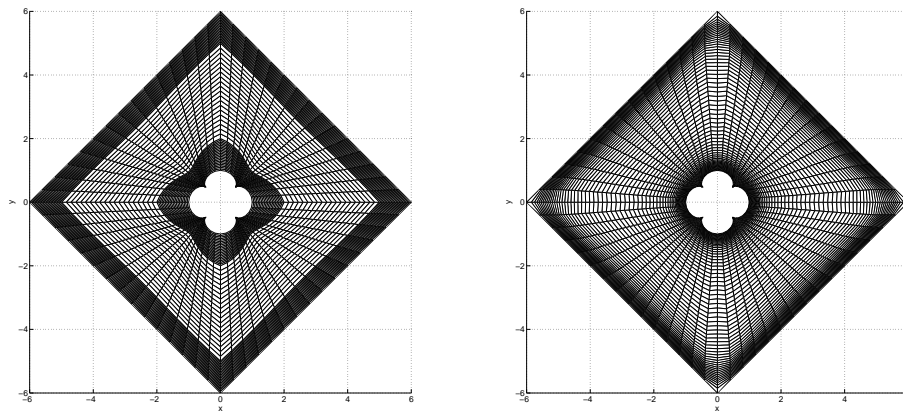

FIGURE 7.2. *Initial algebraic grid and final* 61×61 *mixed algebraic-$\alpha\gamma$ grid.*

around the complex boundaries. Also, a smooth transition for the separation of the η-curves along the ξ-direction, from the near boundary elliptic grid cells to the algebraic grid cells of the intermediate regions, is observed.

As a final experiment, we construct mixed grids for the multiply-connected region consisting of a NACA2412 airfoil as the inner boundary and an ellipse as the outer boundary; see Figure 7.5. Most algebraic grids overlap at the airfoil trailing edge even for modest grid sizes. In Figure 7.6, a zoom on the airfoil trailing edge for 121×121 initial and mixed algebraic-J grids is shown. Values of the Jacobian at the cell containing the trailing edge are $J_{1,1} = -7.29 \times 10^{-9}$ for the initial algebraic grid, $J_{1,1} = 1.94 \times 10^{-5}$ for the mixed algebraic-$\alpha\gamma$ grid, and $J_{1,1} = 4.79 \times 10^{-5}$ for the mixed algebraic-J grid. The negative sign of $J_{1,1}$ for the cell of the trailing edge indicates an overlapping of cells. This anomaly is fixed by applying the J-grid and $\alpha\gamma$-grid algorithms about the trailing edge starting with this initial grid. Again, the initial grid cell areas and line spacings are enhanced by the application of the
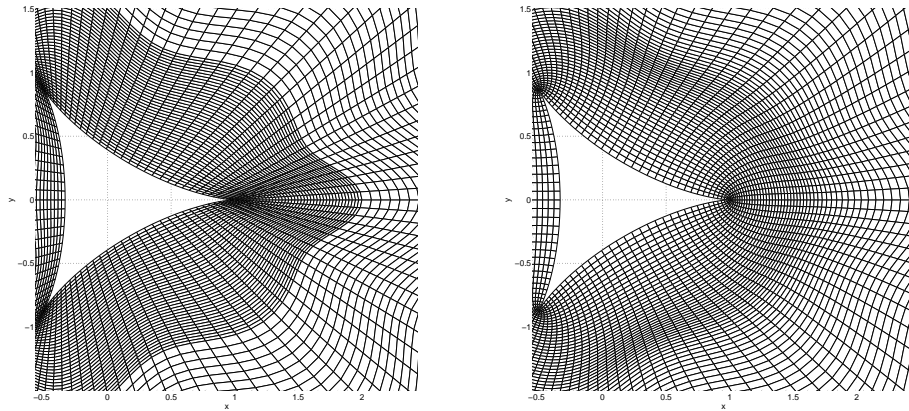
FIGURE 7.3. *Zoom of* 121×121 *initial algebraic grid (left) and final mixed algebraic-J grid (right).*
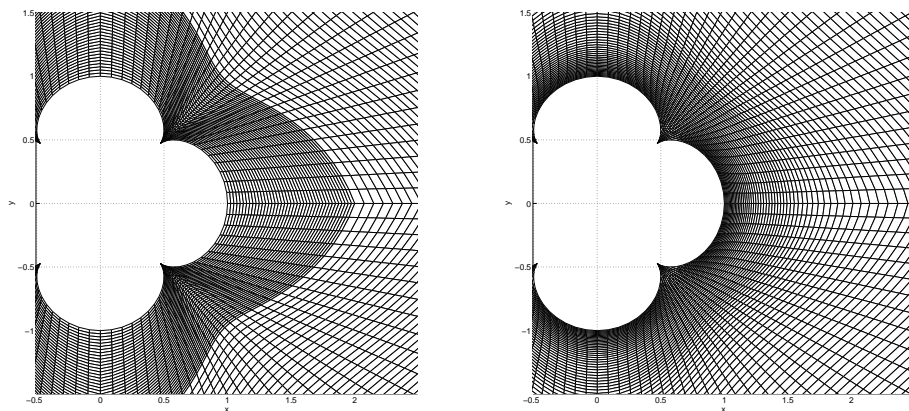

FIGURE 7.4. *Zoom of* 121×121 *initial algebraic grid (left) and final mixed algebraic-$\alpha\gamma$ grid (right).*
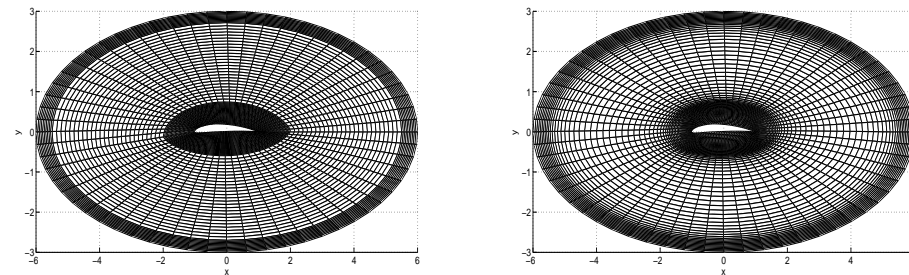

FIGURE 7.5. *Initial algebraic* 61×61 *grid (left) and mixed algebraic-J-grid (right) around a NACA2412 airfoil.*
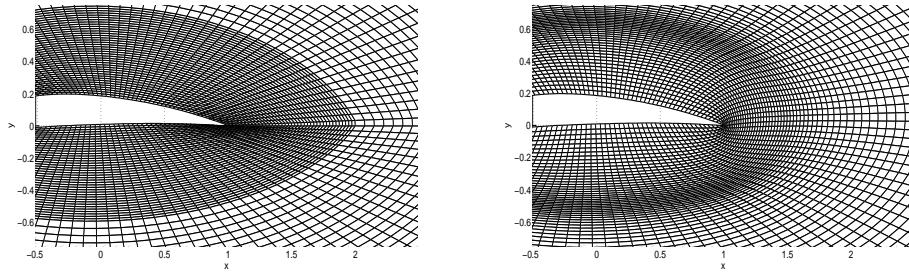
FIGURE 7.6. *Zoom on* 121×121 *initial algebraic and mixed grids for the NACA2412 airfoil at the trailing edge.*

new techniques.

8. Conclusions. The commonly used elliptic grid generation system given by (2.1)–(2.2) has been extended to four elliptic equations. The new models exploit the geometric properties of the Jacobian J (cell area) and the metric factors α (grid line separation along the η-direction) and γ (grid line separation along the ξ-direction) for their formulations.

The key aspect in the formulation of the two new equations is the knowledge that increasing (decreasing) values of the control functions ϕ and ψ of the classical elliptic system produces relocation of the grid lines in the positive direction (negative direction) along the η-direction and ξ-direction, respectively.

It is seen from the various domains considered in this work that the final grid is the ultimate product of a series of adjustments of ϕ and ψ during an iterative process. These adjustments obey to the need of minimizing the area or line spacing differences between cells without sacrificing the boundary conforming property.

The main difference between the elliptic generation technique proposed in this work and known elliptic methods is that the control functions ϕ and ψ are completely unknown and the generation is fully automatic. They are not defined before the generation starts as in [10, 11, 13, 14, 19, 20]. They are not modified to minimize errors of supported field computation as in [9]. If a specific distribution of grid points (such as special clustering or stretching of grid lines) is not required anywhere in the domain being discretized, then J and $\alpha\gamma$-grids constitute a good choice because of their enhanced properties in terms of near uniformity of cell area and line spacing. Nevertheless, one should notice a natural appearance of a cluster of η-curves in a neighborhood of the inner boundaries for $\alpha\gamma$-grids. However, the distance among the η-curves does not grow as much as for other elliptic generators away from the inner boundaries. This is due to the tendency of the $\alpha\gamma$-grids to preserve the grid line separations.

The two-dimensional grid generation algorithm introduced in this work can be naturally extended to three-dimensional domains. To start, consider the classical two-dimensional algorithm formed by (2.1)–(2.2). In three dimensions, a natural extension consists of adding a third elliptic equation for the physical coordinate z and a third computational variable ζ. Also, a third control function Λ is needed for three-dimensional elliptic grid generators. The corresponding metric factors and the Jacobian J have geometrical interpretations, such as surface separation and cell volume, respectively. Detailed formulations are found in [8, 10, 16, 18, 19]. They consist of the quasi-linear elliptic system of partial differential

equations given by

$$a_{11}x_{\xi\xi} + a_{22}x_{\eta\eta} + a_{33}x_{\zeta\zeta} + 2(a_{12}x_{\xi\eta} + a_{13}x_{\xi\zeta} + a_{23}x_{\eta\zeta}) = \tag{8.1}$$
$$-a_{11}\,\psi x_\xi - a_{22}\phi\,x_\eta - a_{33}\Lambda\,x_\zeta,$$

$$a_{11}y_{\xi\xi} + a_{22}y_{\eta\eta} + a_{33}y_{\zeta\zeta} + 2(a_{12}y_{\xi\eta} + a_{13}y_{\xi\zeta} + a_{23}y_{\eta\zeta}) = \tag{8.2}$$
$$-a_{11}\psi\,y_\xi - a_{22}\phi\,y_\eta - a_{33}\Lambda\,y_\zeta,$$

$$a_{11}z_{\xi\xi} + a_{22}z_{\eta\eta} + a_{33}z_{\zeta\zeta} + 2(a_{12}z_{\xi\eta} + a_{13}z_{\xi\zeta} + a_{23}z_{\eta\zeta}) = \tag{8.3}$$
$$-a_{11}\psi\,z_\xi - a_{22}\phi z_\eta - a_{33}\Lambda\,z_\zeta,$$

where the a_{ij} $(i,j=1,2,3)$ are the metric factors of the three-dimensional transformation between the computational domain of (ξ,η,ζ) points and the physical domain of (x,y,z) points. Their definitions are found in [16], and the Jacobian is given by

$$J = \begin{vmatrix} x_\xi & x_\eta & x_\zeta \\ y_\xi & y_\eta & y_\zeta \\ z_\xi & z_\eta & z_\zeta \end{vmatrix}.$$

As a second step in the extension of the present algorithms to three dimensions, we add a third term representing the second derivative with respect to ζ to the previous Poisson equations for the control functions ψ and ϕ. Also, a third Poisson equation for the new control function Λ is added to the system. Therefore, the three-dimensional version of the J-algorithm includes the previous equations (8.1)-(8.3) and the following Poisson equation for the control functions

$$\psi_{\xi\xi} + \psi_{\eta\eta} + \psi_{\zeta\zeta} = -k_2 J_\xi, \tag{8.4}$$
$$\phi_{\xi\xi} + \phi_{\eta\eta} + \phi_{\zeta\zeta} = -k_1 J_\eta, \tag{8.5}$$
$$\Lambda_{\xi\xi} + \Lambda_{\eta\eta} + \Lambda_{\zeta\zeta} = -k_3 J_\zeta. \tag{8.6}$$

A completely analogous extension can be carried out for the formulation of the three-dimensional $\alpha\gamma$ algorithm. The actual implementation of these algorithms for three-dimensional domains will be the subject of a forthcoming publication.

The novel grids derived here may be very appropriate for computation on complex domains if they are combined with other grid-types as shown in Section 7. Recently, we have successfully used them to support the pressure field computation in acoustic scattering from an obstacles with complex shapes [3]. Due to their attractive features (smoothness, non-self-overlapping, nearly uniform cell area or nearly uniform line spacing) and their relatively simple implementation, we are confident that these grids will be a great aid to accurate field computations in important problems in applied areas such as fluids and waves.

REFERENCES

[1] S. ACOSTA AND V. VILLAMIZAR, *Acoustic scattering approximations on elliptive grids with adaptive control functions*, in Proc. 8th Int. Conference on Mathematical and Numerical Aspects of Waves, Waves 2007, Reading, UK, 2007, pp. 514–516.

[2] ———, *Grid generation with grid line control for regions with multiple complexly shaped holes*, in Proceedings MASCOT06-IMACS/ISGG Workshop, F. Pitella and R. M. Spitaleri, eds., IMACS, Rome, Italy, 2007, pp. 1–12.

[3] ———, *Acoustic scattering based on elliptic grids preserving cell area and line spacing*, preprint, 2008.

[4] ———, *Generation of smooth grids with line control for scattering from multiple obstacles*, Math. Comput. Simulation, to appear, 2009.

[5] V. AKCELIK, B. JARAMAZ, AND O. GHATTAS, *Nearly orthogonal two-dimensional grid generation with aspect ratio control*, J. Comput. Phys., 171 (2001), pp. 805–821.

[6] J. R. CHAWNER AND J. P. STEINBRENNER, *Automatic structured grid generation using GRIDGEN, surface modeling grid generation, and related issues in computational fluid dynamic (CFD) solutions*, in NASA-CP-3291, Y. K. Choo, ed., 1995, pp. 463–476.

[7] L. ECA, *2D orthogonal grid generation with boundary point distribution control*, J. Comput. Phys., 125 (1996), pp. 440–453.

[8] G. A. HANSEN, R. W. DOGLASS, AND A. ZARDECKI, *Mesh Enhancement*, Imperial College Press, London, 2005.

[9] L. KANIA, *Elliptic adaptive grid generation and area equidistribution*, Internat. J. Numer. Methods Fluids, 30 (1999), pp. 481–491.

[10] S. KIM, *Control functions and grid qualities measurements in the elliptic grid generation around arbitrary surfaces*, Internat J. Numer. Methods Fluids, 33 (2000), pp. 81–88.

[11] P. KNUPP, *Jacobian-weighted elliptic grid generation*, SIAM J. Sci. Comput., 17 (1996), pp. 1475–1490.

[12] P. KNUPP AND N. ROBIDOUX, *A framework for variational grid generation: conditioning the Jacobian matrix with matrix norms*, SIAM J. Sci. Comput., 21 (2000), pp. 2029–2047.

[13] P. KNUPP AND S. STEINBERG, *Fundamentals of Grid Generation*, CRC Press, Boca Raton, Florida, 1993.

[14] S. H. LEE AND B. K. SONI, *The enhancement of an elliptic grid using appropriate control functions*, Appl. Math. Comput., 159 (2004), pp. 809–821.

[15] S. SHERER AND M. VISBAL, *High-order overset-grid simulations of acoustic scattering from multiple cylinders*, in Procedings of the Fourth Computational Aeroacoustics (CAA) Workshop on Benchmark Problems, NASA/CP-2004-212954, 2004.

[16] C. SHIEH, *Three-dimensional grid generation using elliptic equations with direct grid distribution control*, AIAA Journal, 22 (1984), pp. 361–364.

[17] J. L. STEGER AND R. L. SORENSON, *Automatic mesh point clustering near a boundary in grid generation with elliptic partial differential equations*, J. Comput. Phys., 33 (1979), pp. 405–410.

[18] J. F. THOMPSON, *A general three-dimensonal elliptic grid generation system on a composite block structure*, Comput. Methods Appl. Mech. Engrg., 64 (1987), pp. 377–411.

[19] J. F. THOMPSON, B. K. SONI, AND N. G. WEATHERILL, *Handbook of Grid Generation*, CRC Press, Boca Raton, Florida, 1999.

[20] V. VILLAMIZAR, O. ROJAS, AND J. MABEY, *Generation of curvilinear coordinates on multiply connected regions with boundary singularities*, J. Comput. Phys., 223 (2007), pp. 571–588.

[21] V. VILLAMIZAR AND M. WEBER, *Boundary-conforming coordinates with grid line control for acoustic scattering from complexly shaped obstacles*, Numer. Methods Partial Differential Equations, 23 (2007), pp. 1445–1467.

[22] A. WINSLOW, *Numerical solution of the quasilinear poisson equations in a nonuniform triangle mesh*, J. Comput. Phys., 2 (1967), pp. 149–172.